ISSN 1560-3547, Regular and Chaotic Dynamics, 2018, Vol. 23, No. 3, pp. 257–272. © Pleiades Publishing, Ltd., 2018.

Nonlinear Dynamics of a Bubble Contrast Agent Oscillating near an Elastic Wall

Ivan R. Garashchuk*, Dmitry I. Sinelshchikov, and Nikolay A. Kudryashov*****

National Research Nuclear University MEPhI,
Kashirskoe sh. 31, Moscow, 115409 Russia

Received February 05, 2018; accepted March 23, 2018

Abstract—Contrast agent microbubbles, which are encapsulated gas bubbles, are widely used to enhance ultrasound imaging. There are also several new promising applications of the contrast agents such as targeted drug delivery and noninvasive therapy. Here we study three models of the microbubble dynamics: a nonencapsulated bubble oscillating close to an elastic wall, a simple coated bubble and a coated bubble near an elastic wall. We demonstrate that complex dynamics can occur in these models. We are particularly interested in the multistability phenomenon of bubble dynamics. We show that coexisting attractors appear in all of these models, but for higher acoustic pressures for the models of an encapsulated bubble. We demonstrate how several tools can be used to localize the coexisting attractors. We provide some considerations why the multistability can be undesirable for applications.

MSC2010 numbers: 37N10, 34A34, 37N25

DOI: 10.1134/S1560354718030036

Keywords: contrast agent, dynamical system, nonlinear dynamics, dynamical chaos, multistability, coexisting attractors

1. INTRODUCTION

Ultrasound contrast agents are encapsulated gas bubbles with radius on the order of a few micrometers [1–3]. They are currently widely used in ultrasound visualization [1–3]. Such bubbles are injected into blood stream to enhance acoustic contrast between the blood and the surrounding tissues. There are also several promising new applications of microbubbles such as targeted drug delivery and noninvasive therapy [4, 5]. Therefore, mathematical modelling of the dynamics of contrast agent microbubbles is an important problem.

Almost all mathematical models of the contrast agents dynamics are based on the Rayleigh equation for the growth and collapse of an empty spherical cavity in a liquid [6]. Later this equation was generalized to include into consideration fluid viscosity and the gas core of a bubble [7]. This model is now called the Rayleigh – Plesset equation. After practical usage of first contrast agents, which were unshelled, it has become clear that in order to improve their stability it is necessary to use encapsulated bubbles [8]. This has led to development of mathematical models of coated bubbles (see, e. g., [9] and references therein). All of the above-mentioned models are one-dimensional oscillators, which usually include periodic force that describes an external acoustic pressure field. Thus, such models are three-dimensional dynamical systems in which complex dynamics can occur.

Although there are a lot of models for the description of encapsulated bubbles dynamics which are suitable for different types of shells and different situations, only few of them were thoroughly studied from the dynamical systems point of view. We can mention the works [10, 11], where the dynamics of the unshelled bubbles was considered. In [12, 13] the case of encapsulated bubbles was studied. However, in [12] an inappropriate model of the shell was considered (see [9] for a

*E-mail: ivan.mail4work@yandex.ru
**E-mail: disine@gmail.com
***E-mail: nakudr@gmail.com

discussion), while in [13] fluid compressibility was not fully taken into account and only one model of the shell was considered. In addition, there is a new model of bubbles dynamics which takes into account the impact of an elastic wall near which a bubble oscillates [14]. As far as analytical studies of the models of bubbles dynamics are concerned, one can mention the works [15–17], though in these studies nondissipative cases were considered. Thus, it is interesting to thoroughly study a model of bubble dynamics which fully incorporates fluid compressibility, bubble's shell and the impact of an elastic wall. This is the main aim of this work.

Firstly, we consider a model of bubble dynamics without taking into account the influence of its shell. We provide a discussion of this model for the sake of comparison with later ones. Secondly, we investigate a model for a simple coated bubble. We use the de-Jong approach (see [9, 18, 19]) to describe the impact of the shell on the dynamics. Although this model is quite simple and cannot represent some effects arising in real bubbles dynamics (like the compression-only behavior, for details see the discussion in [9]), it can fairly well describe the effects connected with the shell when its thickness is small in comparison with the bubble diameter. In addition, there are a lot of parameters available for different types of contrast agents for this model (see, e. g., [20]), which are often hard or impossible to find for some more complicated models because of lack of experimental data. Lastly, we study a model that incorporates the influence of both the shell and the wall near which the bubble is oscillating. We show that in both models of encapsulated bubble dynamics complex dynamics may occur. In particular, we show the possibility of coexistence of attractors in these models. For a detailed discussion, see Section 4. In the last section we briefly summarize and discuss our results.

2. MATHEMATICAL MODELS

In this section we provide three models of the bubble contrast agents, which are studied in this work. In all of them we take into account fluid viscosity and compressibility in accordance with the Keller – Miksis model [21]. The applied ultrasound field is described by the periodic external pressure field in the equations considered. The impact of the shell is taken into account according to the de Jong model [18, 19].

For the nonshelled bubble we investigate the following equation [9, 22]:

$$\left(1-\frac{1}{2}W-\frac{\dot R}{c}\right)R\ddot R+\frac{3}{2}\left(1-\frac{2}{3}W-\frac{\dot R}{3c}\right)\dot R^2=\rho_1\left[1+\frac{\dot R}{c}+\frac{R}{c}\frac{d}{dt}\right]\big(P-P_{ac}\sin(\omega t)\big),\qquad(2.1)$$

where

$$W=\frac{(\rho_1-\beta)\,R}{(\rho_1+\beta)\,d}+\frac{(\beta-\rho_3)\,R}{(\beta+\rho_3)\,(d+h)}-\frac{(\rho_1-\beta)\,(\beta-\rho_3)\,R}{(\rho_1+\beta)\,(\beta+\rho_3)\,h},\qquad(2.2)$$

$$P=\left(P_0+\frac{2\sigma}{R_0}\right)\left(\frac{R_0}{R}\right)^{3\gamma}-\frac{4\eta\dot R}{R}-\frac{2\sigma}{R}-P_0,$$

R is the bubble radius, $P_{\rm stat}=100$ kPa is the static pressure, $P_v=2.33$ kPa is the vapor pressure, $P_0=P_{\rm stat}-P_v$, P_{ac} is the magnitude of the pressure of the external field, $\sigma=0.0725$ N/m is the surface tension, $\rho_1=1000$ kg/m^3 is the density of the fluid inside the blood vessel, $\rho_2=1060$ kg/m^3 is the blood vessel wall density, $\rho_3=1000$ kg/m^3 is the density of the fluid surrounding the blood vessel, $\eta=0.001$ Ns/m^3 is the viscosity of the fluid, $c=1500$ m/s is the sound speed, $\gamma=4/3$ is the polytropic exponent (the process is assumed to be adiabatic), ν is the Poisson ratio, $\nu=0.5$ for an elastic wall, and $\nu=0$ for a rigid wall, $\beta=\rho_2\nu/(1-\nu)$ is a characteristic of the wall, $h=1$ mm is the thickness of the wall, d denotes the distance between the wall and the center of the bubble and is close to R_0.

For the encapsulated bubble, we consider two models. The first one that does not include the influence of an elastic wall is

$$\left(1-\frac{\dot R}{c}\right)R\ddot R+\frac{3}{2}\left(1-\frac{\dot R}{3c}\right)R_t^2=\rho\left[1+\frac{\dot R}{c}+\frac{R}{c}\frac{d}{dt}\right]\big[P-P_{ac}\sin(\omega t)\big],\qquad(2.3)$$

where

$$P = \left(P_0 + \frac{2\sigma}{R_0}\right)\left(\frac{R_0}{R}\right)^{3\gamma} - \frac{4\eta_L \dot{R}}{R} - \frac{2\sigma}{R} - P_0 - 4\chi\left(\frac{1}{R_0} - \frac{1}{R}\right) - 4\kappa_S \frac{\dot{R}}{R^2}$$

and the second one, which includes the impact of an elastic wall, is

$$\left(1 - \frac{1}{2}W - \frac{\dot{R}}{c}\right) R\ddot{R} + \frac{3}{2}\left(1 - \frac{2}{3}W - \frac{\dot{R}}{3c}\right)\dot{R}^2 = \frac{1}{\rho_1}\left[1 + \frac{\dot{R}}{c} + \frac{R}{c}\frac{d}{dt}\right]\left(P - P_{ac}\sin(\omega t)\right), \quad (2.4)$$

where P is the same as in the previous case, and W is given by (2.2). In Eqs. (2.3) and (2.4) all parameters are the same as in Eq. (2.1) with the exception of χ and κ_s, which denote the shell elasticity and shell surface viscosity, respectively. We use the following values of these parameters: $\chi = 0.22$ N/m and $\kappa_S = 2.510^{-9}$ kg/s, which correspond to the SonoVue® contrast agent with equilibrium radius $R_0 = 1.72$ μm [20].

In this work we focus on the multistability phenomenon in Eqs. (2.1), (2.3) and (2.4). In other words, we investigate the possibility of coexistence of several attractors at the same values of the control parameters in these models. An attractor is called hidden if its basin does not intersect with any small neighborhood of a fixed point [23]. Thus, such an attractor cannot be found by picking the initial data in a neighborhood of an unstable fixed point. One can note that all the dynamical systems corresponding to Eqs. (2.1), (2.3) and (2.4) do not have any fixed points. Consequently, all the attractors are hidden according to the definition. If there is only one attractor for the given parameter value, the system will converge to it from any initial conditions (if they are acceptable for the model). But in the instance of coexistence of multiple attractors, the initial values problem becomes nontrivial.

One of the tools we try to apply to localize coexisting attractors is the perpetual points method [23, 24]. However, below we show that it does not give us the desirable results for the physically relevant values of the control parameters. Perpetual points are defined by the following system of equations:

$$\ddot{R} = 0, \quad \dddot{R} = 0, \quad (2.5)$$

which are rational equations with respect to $R, \dot{R}$. Equations (2.5) are periodic with respect to time with period $T = 2\pi/\omega$. Consequently, we solve this system for the entire time period with a sufficiently small time step to find out if the number of solutions would be different for any specific time in this interval. Our aim at this point is to find the time values for which the number of solutions would be the highest. However, for Eqs. (2.5), corresponding to (2.1) and (2.4), the number of solutions remains almost the same on the whole interval, starting from $t = 0$, except for some specific time values for which no solutions exist at all. For all the parameter values for which we have calculated the perpetual points, the maximum number of solutions was always the same as calculated at time $t = 0$.

Another method we use here for localizing coexisting attractors is based on the numerical continuation [25–28]. According to this idea, we take the state of the system at the last time step of computation for current values of the parameters as the initial conditions for the next calculation with respect to the control parameters. If the step size between the consequent parameter values is small enough, the system should not switch from one attractor to another, because deformation of the basins of attractors should not be large enough for this to happen. However, this might not always be true if a bifurcation point is passed on the path variation of the control parameters (see [25]). On the other hand, if the step size is not sufficiently small, it becomes possible for the initial data chosen in this way (in a small neighborhood of the attractor for the current parameter value) to find themselves in the basin of another attractor for the next value of the control parameters.

Throughout this work, for all numerical calculations the fourth-fifth order Runge – Kutta method is used [29]. We have compared the results of calculations with those of [12] and have found satisfactory agreement. For the calculations of the Lyapunov spectra we use the standard algorithm by Bennetin [30]. We have tested our numerical code on the results of [31] for the driven Van-der-Pol oscillator and the Lorentz system and have found satisfactory agreement. Note that all

calculations have been performed in the following nondimensional variables $R = R_0 R^*$, $t = \omega_0^{-1}\tau$, where $\omega_0^2 = 3\kappa P_0/(\rho R_0^2) + 2(3\kappa - 1)\sigma/R_0 + 4\chi/R_0$ is the natural frequency of bubble oscillations. We denote the nondimensional radial speed as R_τ^*. Here, and throughout the remainder of the text, we denote the largest of the Lyapunov exponents by $\lambda_{\max}$. We provide only $\lambda_{\max}$, because, given the structure of the system, one of the exponents is always zero, while the sum of the other two must be below zero, because the systems considered are dissipative. Thus, the sign of $\lambda_{\max}$ gives us the criterion of the presence of chaos in the system. We provide the $\lambda_{\max}$ for the nondimensional system, as we are interested only in the sign of the $\lambda_{\max}$.

3. A NONENCAPSULATED BUBBLE CASE

In this section, we consider the nonshelled bubble model corresponding to Eq. (2.1). For the uncoated bubble we use the following equilibrium bubble radius: $R_0 = 10$ μm [10]. We investigate two different control parameter regions, where one can observe the multistability in the model. The first of them is $P_{ac} = 90$ kPa, $\omega/2\pi \in [110, 125]$ kHz. We seek for the perpetual points in the following subset of the initial conditions space: $0 < R, R < 50 \cdot R_0, |\dot{R}| < c$. Multiplier 50 is quite arbitrary, but it is relatively clear that our model is not applicable for larger initial radii, on the other hand, we wanted it to be large enough for us not to lose generality. In this area of the control parameters, we can obtain only one perpetual point in this subset. One can note that there is one more solution of the system (2.5) for these values of the control parameters, which is located in a neighborhood of infinity compared to the subset mentioned above ($R \sim 2.5 \cdot 10^3 R_0$ for this solution). But we cannot use such points as initial conditions to numerically solve Eq. (2.1). However, there are two coexisting attractors in this area of parameters. Thus, we cannot obtain all of the coexisting attractors by means of the perpetual points method.

The system has the following attractors for these parameters: there are two periodic attractors if $\omega/2\pi \lesssim 110$ kHz and $\omega/2\pi \gtrsim 125$ kHz, one of which is 1-periodic and the other is 2-periodic. If we decrease the frequency from the higher end, the 2-periodic attractor goes through the period-doubling cascade and becomes chaotic, then at approximately 110 kHz it becomes 2-periodic again (see Fig. 1), while the 1-periodic attractor remains almost the same in this entire set of parameters. $\lambda_{\max}$ for different attractors are shown in Fig. 2. One perpetual point that we have here for any given frequency always leads us to the same attractor — the one which goes through the period-doubling cascade.

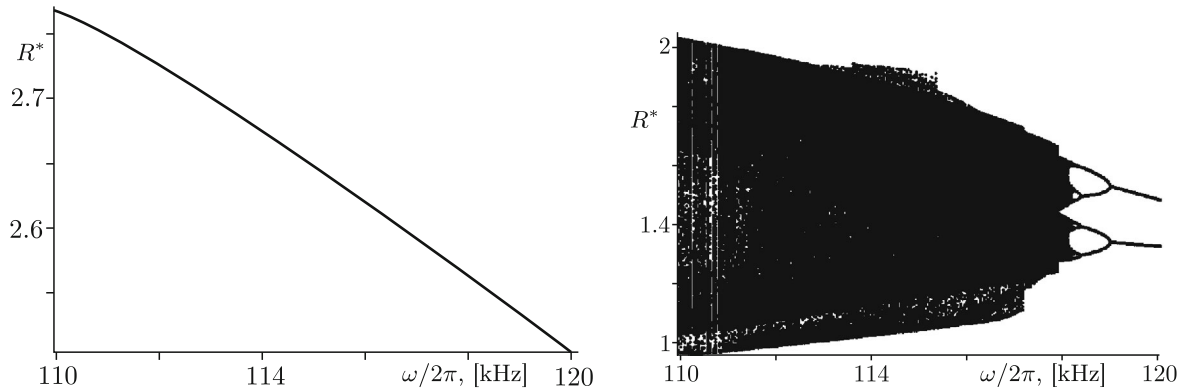

Fig. 1. Bifurcation diagrams for $P = 90$ kPa, $\omega/2\pi \in [110, 120]$ kHz. 1-periodic attractor (left) and the periodid-doubling cascade for the 2-periodic attractor (right).

Thus, we need some more tools to localize all the attractors. Here we use the numerical continuation approach. The step size by the control parameter is an important issue with this method. Our experiments show that if we choose the step size so that the adjacent frequencies in the diagram differ by $\sim 1\%$, the deformation of the attractor basins can be large enough for the system to switch from chaotic motion to periodic and vice versa for the consequent values of the frequencies (see [32]). If we consider a physically realistic system in which there always exist finite perturbations and errors in measurements of the control parameters, we can treat our step size as

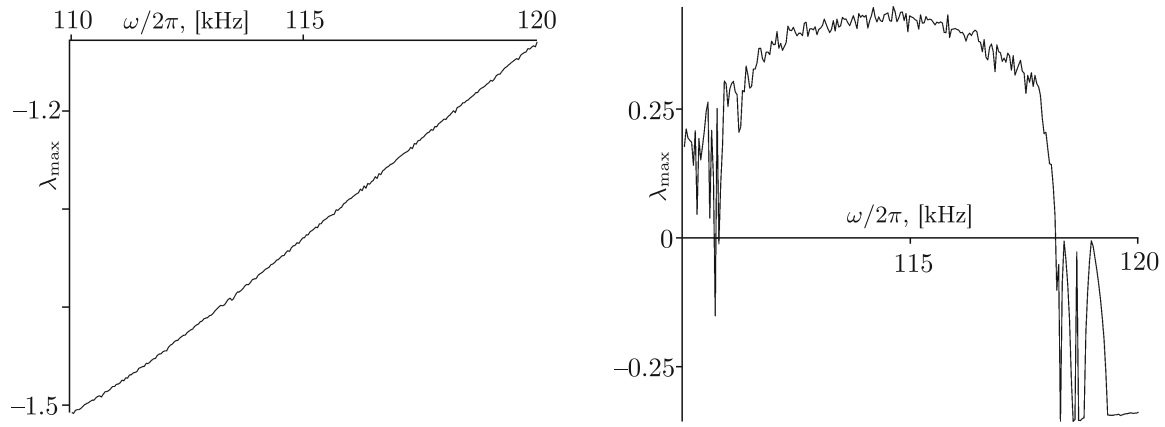

Fig. 2. $\lambda_{\max}$ for the 1-periodic attractor (left) and the chaotic one (right).

a finite disturbance in the system. We can conclude that if these perturbations are relatively large, it can lead to an unpredictable behavior: the system can suddenly shift from chaotic motion to periodic and vice versa. We consider this effect to be undesirable for applications.

The bifurcation diagrams built by means of the numerical continuation method are shown in Fig. 1. Here we used the decreasing frequency sequence, and the step size is such that the difference between neighboring frequencies is about $\approx 0.3\%$. As the initial data for the first calculation we used a point leading to a certain attractor. For the 2-periodic attractor we used the perpetual point obtained earlier. And for the 1-periodic attractor we used an experimentally obtained initial condition that converges to this attractor. The diagram with the period-doubling cascade can be obtained either way: by using the perpetual points or with the numerical continuation. On the other hand, we can achieve the diagram corresponding to the 1-periodic attractor only with the numerical continuation as a result of the lack of the perpetual point that leads to this attractor.

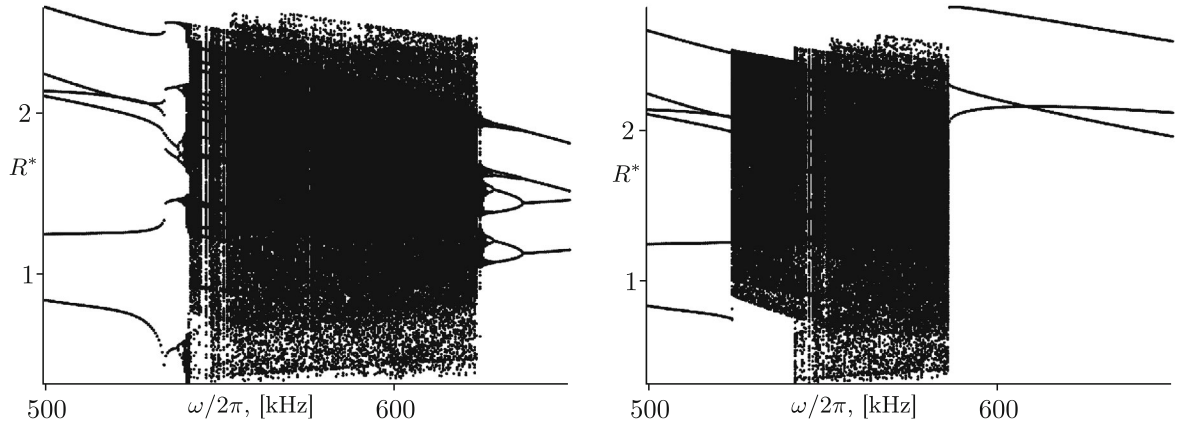

Fig. 3. Bifurcation diagrams for different attractors, 500 kHz $\leqslant \omega/2\pi \leqslant$ 650 kHz.

Now let us consider another area of the control parameters: $P_{ac} = 300$ kPa, $\omega/2\pi \in [500, 650]$ kHz. In this interval, we can also see various examples of multistability. For some parameters a chaotic attractor coexists with a periodic one, for some other parameters, two periodic attractors coexist. However, there are no perpetual points at all in a subset of the initial conditions space which we talked about earlier. The bifurcation diagrams and the dependence of the $\lambda_{\max}$ on the ω for these parameter regions are shown in Figs. 3, 4. It can be seen that a chaotic attractor coexists with a periodic one in a wide range of frequencies. For other frequencies, two periodic attractors coexist (like a 2-periodic and a 3-periodic for $\omega/2\pi \approx 630$ kHz, which can be seen from the bifurcation diagram in Fig. 3). The situation in general has some similarities to the one we investigated before. Two periodic attractors coexist, one of which becomes chaotic for certain frequencies, while the

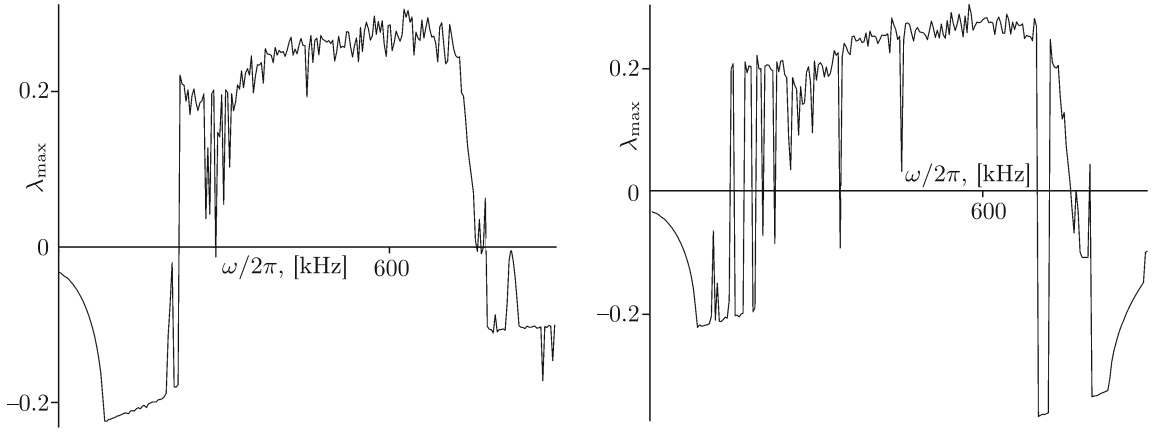

Fig. 4. $\lambda_{\max}$ (left) — for the attractor which undergoes a period-doubling sequence, (right) — oscillations between chaotic and periodic attractors in the multistability zone.

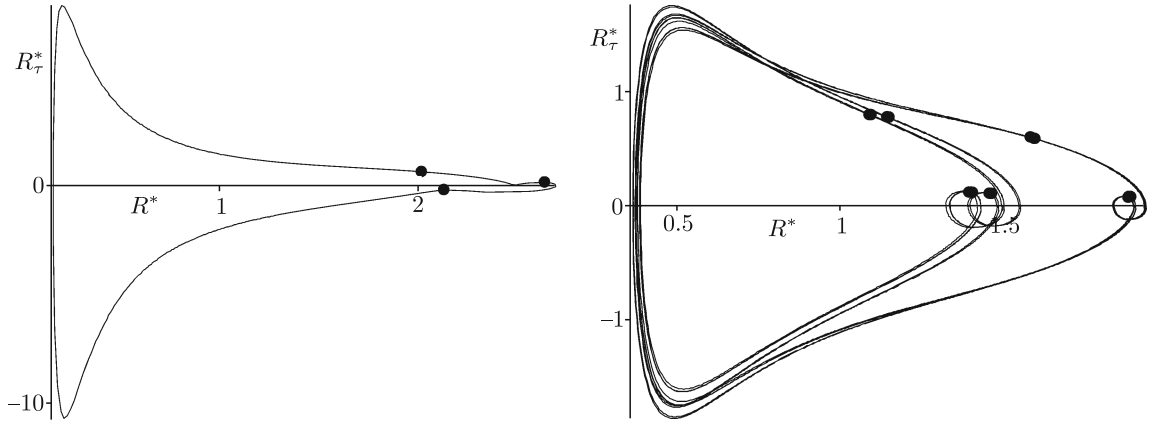

Fig. 5. Coexisting attractors at $P_{ac} = 300$ kPa, $\omega/2\pi = 635$ kHz: 3-periodic attractor (left), 2-periodic after a couple of flip bifuractions (right).

other remains periodic. However, the periodic attractors in this case are more complex (like those in Fig. 5). The transition to chaos with the decreasing frequency for one of the attractors looks like a period-doubling cascade (see Fig. 3).

4. THE CASE OF A BUBBLE ENCAPSULATED IN A SHELL

In this section we investigate Eqs. (2.3) and (2.4) for the dynamics of an encapsulated bubble. As a quick comparison to the previous model, we can make a statement that a shell in general inhibits the emergence of chaos. Thus, chaotic motion in general arises at much higher pressures than in the model described by Eq. (2.1). So does the multistability phenomenon. Below we show that the coexistence of a periodic and a chaotic attractor arises at significantly higher acoustic pressures than we discussed in the previous section. We investigate the following region of the control parameters: $P_{ac} \in [0, 4]$ MPa, $\omega \in [1 \cdot 10^7, 10 \cdot 10^7]$ s^{-1}, because they are meaningful for applications [3]. Let us consider the same subset of the initial conditions space as in the previous section: $0 < R, R < 50 \cdot R_0, |\dot{R}| < c$. Unfortunately, we have not found any perpetual points at all in this subset for either of the two shelled bubble models (2.3), (2.4) in this domain of the control parameters. Consequently, we have to use the continuation tool to seek for coexisting attractors. First, we consider the simpler one.

4.1. Pure de Jong Model

Let us investigate the dynamics of bubbles oscillations described by Eq. (2.3).

We start by studying the dynamics of bubble oscillations described by Eq. (2.3), i. e., we do not take into account the influence of a blood vessel wall. In Fig. 6 we demonstrate bifurcation diagrams with respect to the frequency and magnitude of the acoustic pressure field. In the right area of Fig. 6 we see a sharp change from a 1-periodic attractor to a 3-periodic one. This fact suggests the possibility of coexisting attractors near the corresponding value of ω.

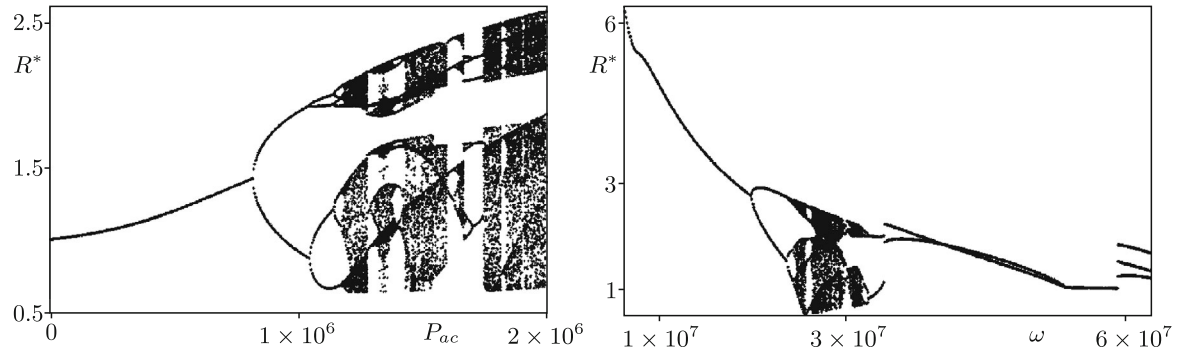

Fig. 6. Bifurcation diagrams for model (2.3) for different values of the acoustic pressure (left) at $\omega/2\pi = 4.7 \cdot 10^6$ and different values of the acoustic frequency (right) at $P_{ac} = 1.5 \cdot 10^6$ Pa.

To support the qualitative results presented in Fig. 6, we demonstrate the dependence of the $\lambda_{\max}$ on the control parameters in Fig. 7. One can see that the value of the $\lambda_{\max}$ demonstrated in Fig. 7 correlates with the regular and chaotic regions in bifurcation diagrams. Note also oscillations of $\lambda_{\max}$ in the right region of the first plot in Fig. 7, which again suggests the possibility of coexistence of two periodic attractors.

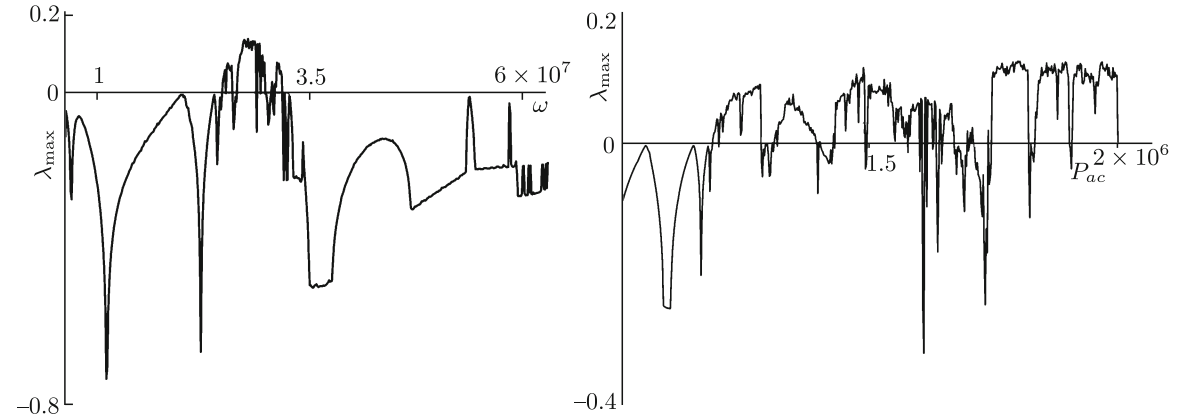

Fig. 7. The dependence of the $\lambda_{\max}$ for model (2.3) for different values of the acoustic pressure (left) at $\omega/2\pi = 4.7 \cdot 10^6$ and different values of the acoustic frequency (right) at $P_{ac} = 1.5 \cdot 10^6$ Pa.

Indeed, in this case two different periodic attractors coexist. In Fig. 8 we demonstrate phase portraits of two different coexisting attractors at $\omega = 1.9\pi \cdot 10^7$ and $P = 1.5 \cdot 10^6$ for two different initial conditions $R(0) = 0.8 \cdot R_0$ (one periodic) and $R(0) = R_0$ (three periodic).

We also demonstrate the dependence of the $\lambda_{\max}$ on the initial bubble strain, i. e., on $R(0)/R_0$, and the initial radial speed R^*_τ.

From Fig. 9 we see that there are two different values of the $\lambda_{\max}$, which corresponds to the existence of two different attractors at the same values of the parameters. Therefore, we can distinguish the coexisting periodic attractors by calculating the dependence of Lyapunov spectra on the initial conditions.

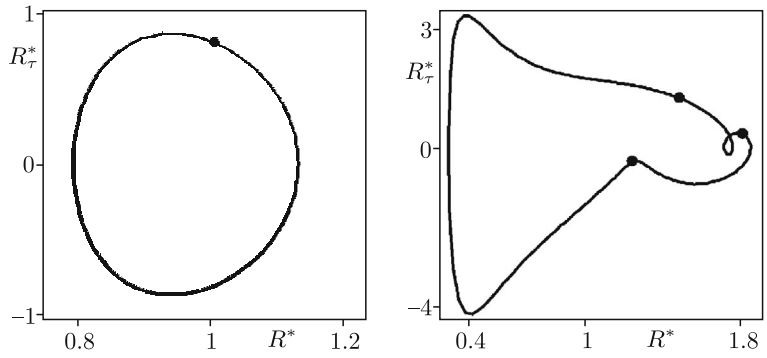

Fig. 8. Phase portraits of two coexisting attractors for model (2.3) at $\omega = (19/20) \cdot 10^7$ and $P = 1.5 \cdot 10^6$: 1-periodic (left) and 3-periodic (right).

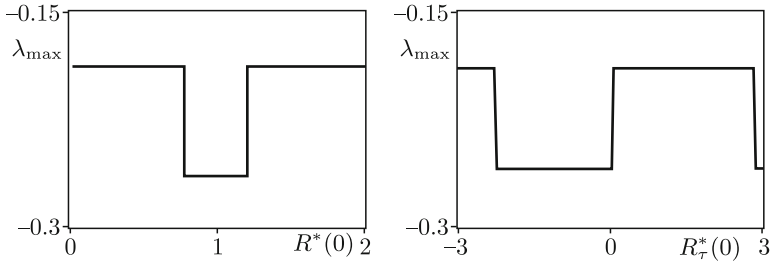

Fig. 9. The dependence of the $\lambda_{\max}$ on the initial bubble strain $R(0)/R_0$ (left) and initial nondimensional bubble speed $R^*_\tau(0)$ (right).

4.2. Encapsulated Bubble Close to an Elastic Wall

Here we investigate the dynamics of a bubble, described by Eq. (2.4), which differs from Eq. (2.3) by the presence of the term corresponding to the interaction with an elastic wall (see (2.2)). Firstly, let us consider the following parameters: $P_{ac} = 1.5$ MPa, $\omega \in [1, 7] \cdot 10^7$ s^{-1}. The bifurcation diagram and the corresponding $\lambda_{\max}$ are provided in Fig. 10. Let us compare the results obtained with the diagram for the same control parameters but for the de Jong model, which is depicted in Fig. 6. The region of chaos in Fig. 10 is shorter than that in Fig. 6, corresponding to model (2.3). The wall slighlty stabilizes the bubble behavior and suppresses chaos for some frequencies. Just as in the previous model, two coexisting attractors can be found here for this value of the acoustic pressure, namely, a 1-periodic and a 3-periodic attractor. The coexistence appears for higher frequencies in the above-mentioned range. It emerges at ω slightly lower than $6 \cdot 10^7$ s^{-1}. The diagram we built here does not have switches from one of the coexisting attractors to another, but we will prove the presence of the multistability a bit later (see Fig. 14). We do not provide a phase portrait of the coexisting periodic attractors here, because they look pretty much the same as those in Fig. 8 (as a result of proximity of the models described by Eqs. (2.4) and (2.3)).

Secondly, we fix the $\omega = 6.9 \cdot 10^7$ (for which 3-periodic and 1-periodic attractors coexist for a wide range of pressures) and vary the acoustic pressure. The bifurcation diagram and the corresponding $\lambda_{\max}$ are provided for $P_{ac} \in [1, 4]$ MPa. The diagrams in Fig. 11 are built with the help of the numerical continuation method for increasing pressure sequences. For the diagram, starting with the 3-periodic attractor, we start from $P_{ac} = 2$ MPa, because the emergence of the 3-periodic attractor for $\omega = 6.9 \cdot 10^7$ happens at pressures slightly lower than 2 MPa (see Fig. 14), and there is no need to pick P_{ac} close to this bifurcation point with high precision as the initial point. We choose the increasing frequencies instead of decreasing ones because we were able to localize both the 1-periodic and the 3-periodic attractor for lower pressures, and we can use them to start the procedure and build the diagrams. However, if we started from $P_{ac} = 4$ MPa, where only a chaotic attractor exists, we would be unable to achieve these diagrams for either of the attractors that exist at lower pressures.

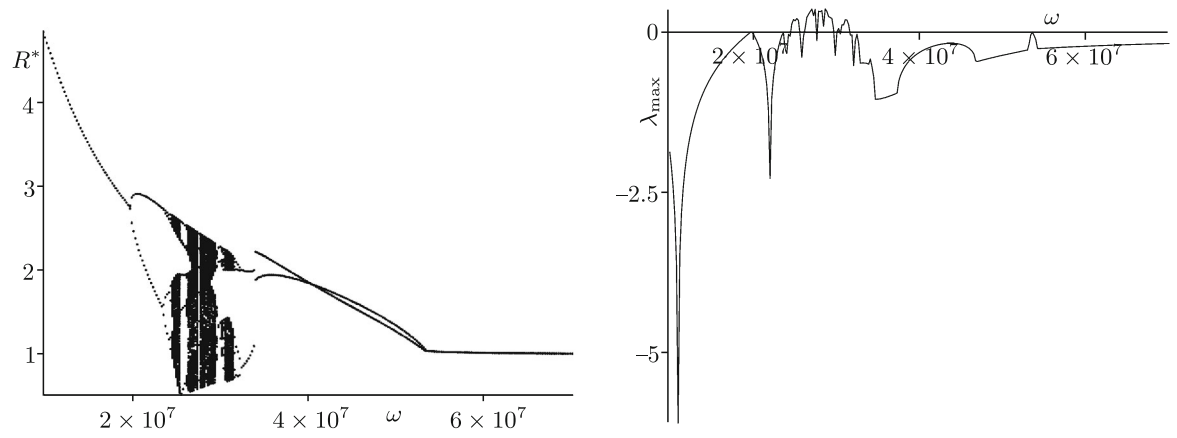

Fig. 10. Bifurcation diagram (left) and $\lambda_{\max}$ (right) for $P = 1.5$ MPa, $\omega \in [1, 7] \cdot 10^7$.

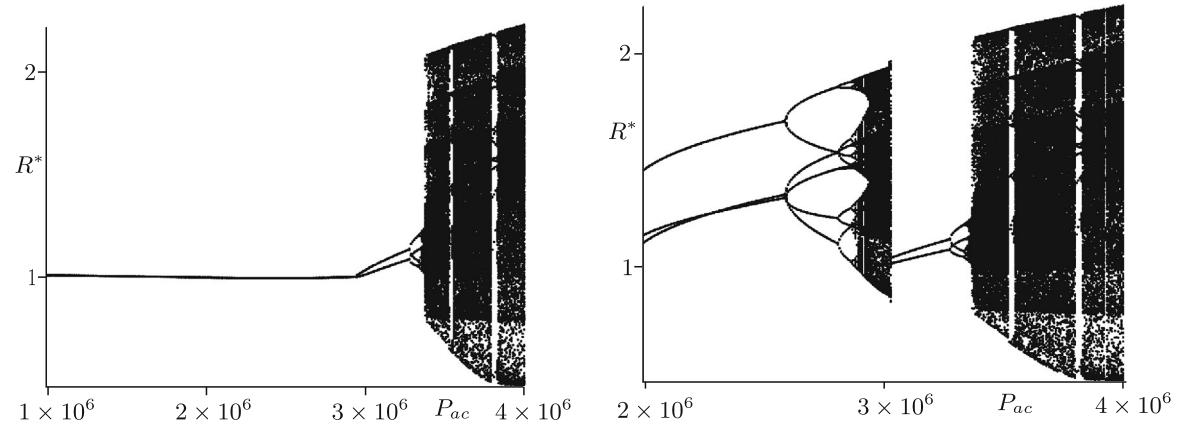

Fig. 11. Bifurcation diagrams for $\omega = 6.9 \cdot 10^7$, left: $P \in [1, 4]$ MPa, right: $P \in [2, 4]$ MPa. Bifurcations of different attractors.

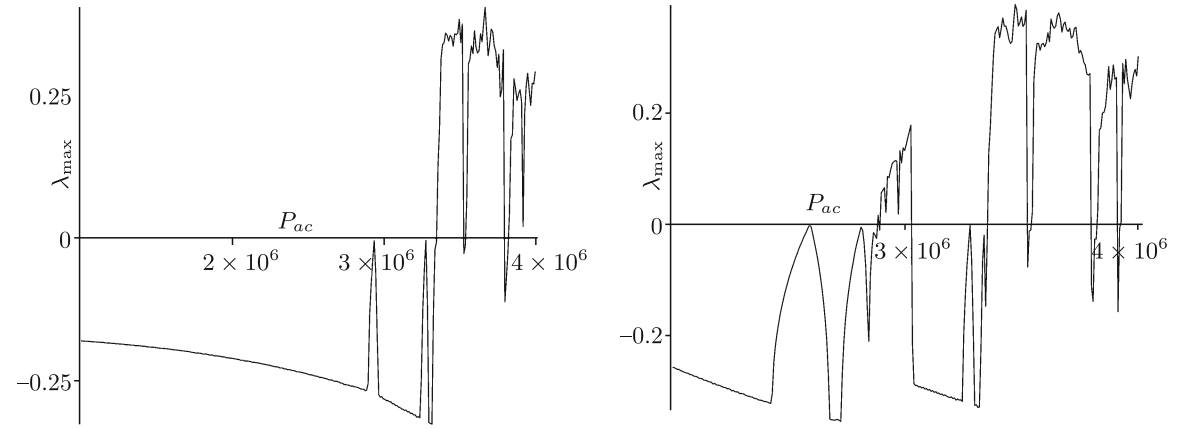

Fig. 12. $\lambda_{\max}$ corresponding to attractors in the bifurcation diagrams in Fig. 11. (left) and (right) correspond to the left and right panels in Fig. 11, respectively.

Here we discover that the 3-periodic attractor undergoes the period-doubling cascade starting at $P_{ac} \approx 2.6$ MPa and becomes chaotic (see Fig. 11). After that, at $P_{ac} \approx 3.02$ it faces a crisis and disappears. For higher pressures we have found only one attractor at this frequency. The 1-periodic attractor remains the same until $P_{ac} \approx 2.94$. At this point the first flip bifurcation of the period-doubling cascade for this attractor occurs. The next bifurcation happens at $P_{ac} \approx 3.3$ MPa.

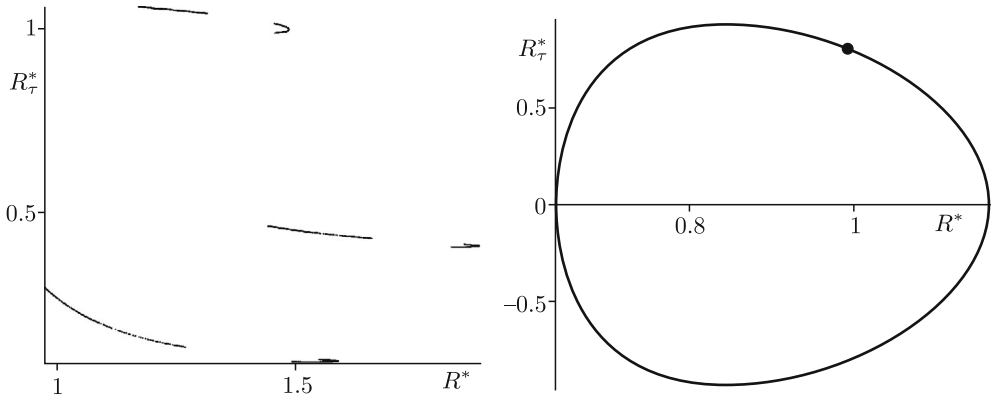

Fig. 13. Coexisting attractors at $P_{ac} = 2.9$ MPa, $\omega = 6.9 \cdot 10^7$ s^{-1}. Poincaré section of the chaotic attractor (left), phase portrait of the 1-periodic attractor (right).

The attractor becomes chaotic after this cascade. There are few windows of regular behavior for higher pressures, though. We have not found any coexisting attractors there. To support these results quantitatively, we have calculated the largest of the Lyapunov exponents (see Fig. 12). As an example of coexisting attractors, we provide the phase portrait of the 1-periodic attractor and the Poincaré section of the chaotic attractor at $P_{ac} = 2.9$ MPa. They are shown in Fig. 13.

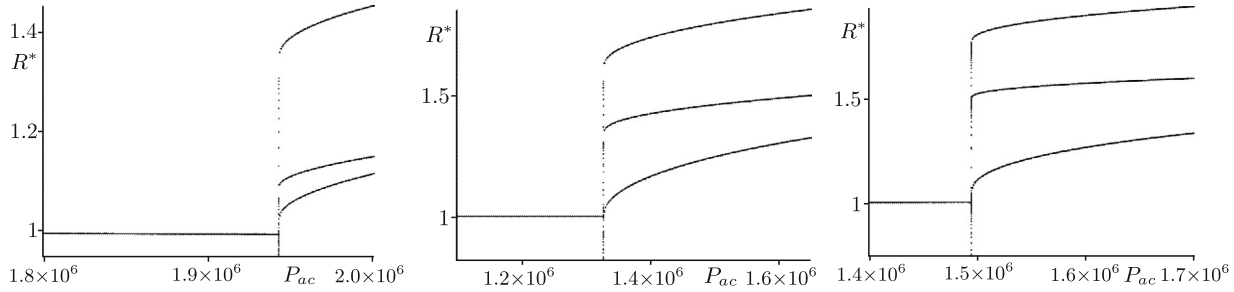

Fig. 14. Bifurcation diagrams showing the emergence of the 3-periodic attractor for different frequencies. Left panel: $\omega = 6.9 \cdot 10^7$ s^{-1}, $P \in [1.8, 2.0]$ MPa, middle panel: $\omega = 6.0 \cdot 10^7$ s^{-1}, $P \in [1.1, 1.65]$ MPa, right panel: $\omega = 5.8 \cdot 10^7$ s^{-1}, $P \in [1.4, 1.7]$ MPa.

To demonstrate the fact of coexistence of the 1-periodic and the 3-periodic attractor for the higher end of frequencies at $P_{ac} = 1.5$ MPa, and also explain the choice of the pressure range for the right panel in Fig. 11, we provide a couple of bifurcation diagrams showing the bifurcation point, where the 3-periodic attractor emerges. To achieve this, we use the decreasing pressure sequences. We know that this attractor exists for the higher pressures for sure from Fig. 11. We can decrease P_{ac} with sufficiently small steps to obtain the point at which the 3-periodic attractor ceases to exist and there will be only the 1-periodic attractor left. The results are shown in Fig. 14. The acoustic pressure for which the 3-periodic attractor emerges depends on the ω in a complicated fashion. This also proves that there is a lower boundary of the pressure under which the multistability does not exist in the model, corresponding to Eq. (2.4), in the set of the control parameters under investigation.

Now we discuss the bifurcation structure for varying acoustic pressures with fixed driving frequencies. Here we consider the following frequencies: $\omega = 2.5 \cdot 10^7$ s^{-1} (see Fig. 15), $\omega = 2.8 \cdot 10^7$ s^{-1} (see Fig. 16), $\omega = 5 \cdot 10^7$ s^{-1} (see Figs. 17), $\omega = 5.5 \cdot 10^7$ s^{-1} (see Figs. 18–20). In Fig. 15 we see a transition to chaos through a period-doubling cascade, which happens at relatively low pressures. It is followed by a window of periodic motion, after which chaos arises again (with a few periodic windows later). We have not found any coexisting attractors here. In Fig. 16 quite a similar picture can be observed, but without such a large periodic window. The scenario happening in Fig. 17 is very similar, but the chaos emerges for much higher pressures. For all three regions of control parameters discussed above, we have not found any multistability. In Figs. 18 and 19 we can observe a much

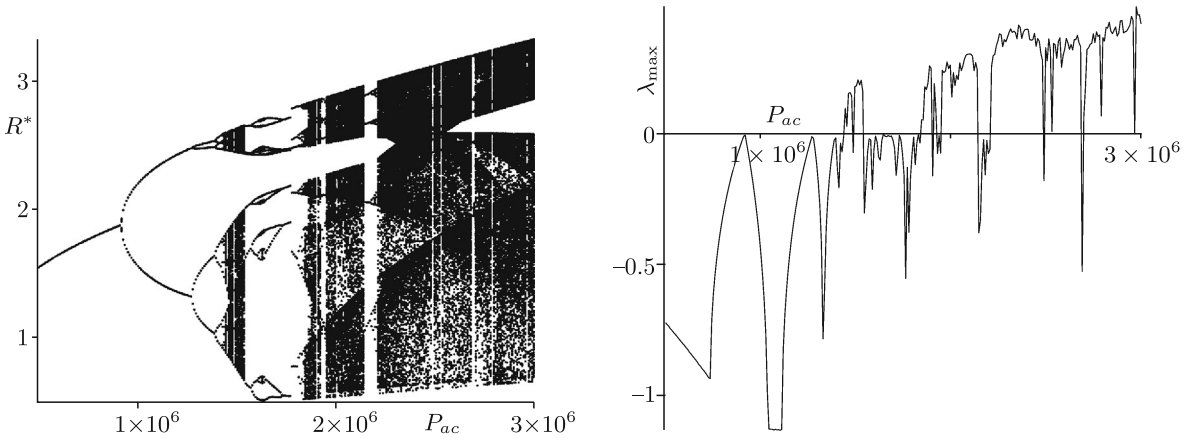

Fig. 15. Bifurcation diagram and $\lambda_{\max}$ for $\omega = 2.5 \cdot 10^7$, $P \in [0.5, 3]$ MPa.

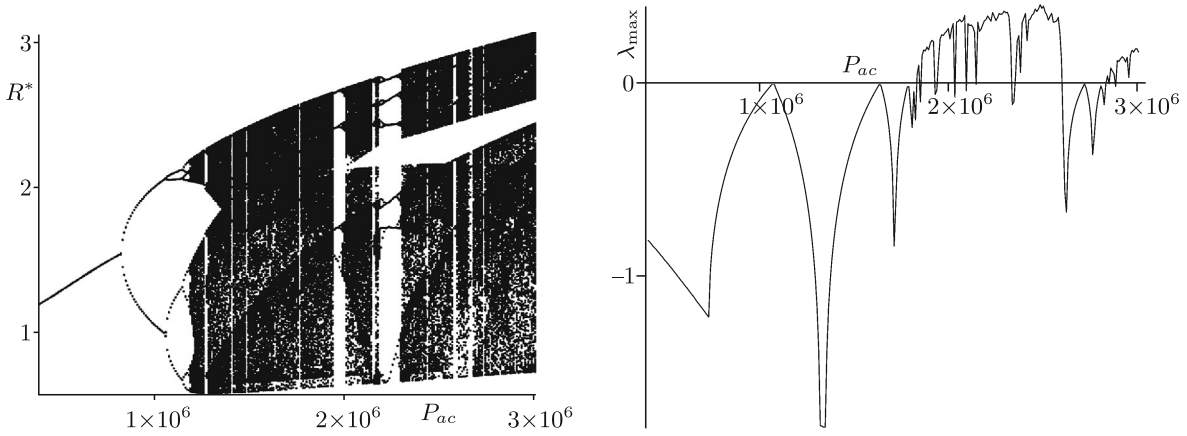

Fig. 16. Bifurcation diagram and $\lambda_{\max}$ for $\omega = 2.8 \cdot 10^7$, $P \in [0.5, 3]$ MPa.

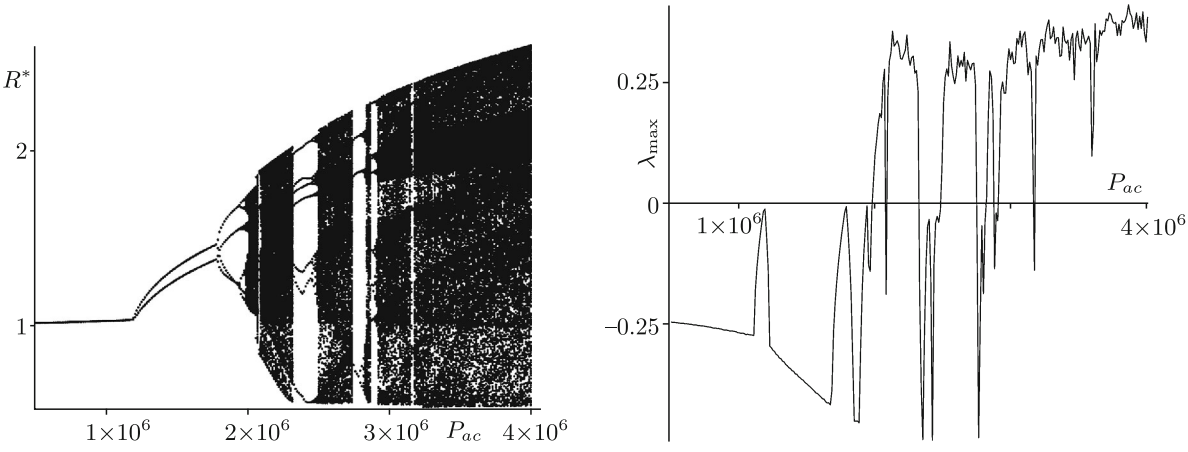

Fig. 17. Bifurcation diagram and $\lambda_{\max}$ for $\omega = 5 \cdot 10^7$, $P \in [0.5, 3]$ MPa.

more complicated situation. In the beginning there is a 1-periodic attractor, which undergoes a flip bifurcation, which is the first one in the period-doubling cascade for this attractor. The next period-doubling bifurcation occurs at $P_{ac} = 2.101$ MPa. For almost the same acoustic pressure a 3-periodic attractor emerges. Note that, although these two bifurcations happen at visually indistinguishable pressures, this does not mean that these points coincide. In our calculations they differ by $\approx 0.4\%$:

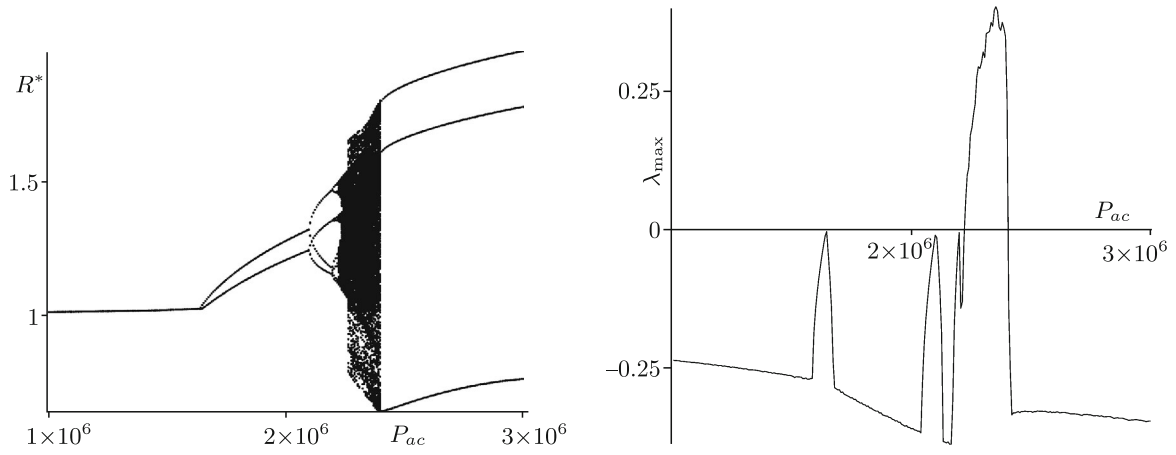

Fig. 18. Bifurcation diagram and $\lambda_{\max}$ for $\omega = 5.5 \cdot 10^7$, $P \in [1, 3]$ MPa.

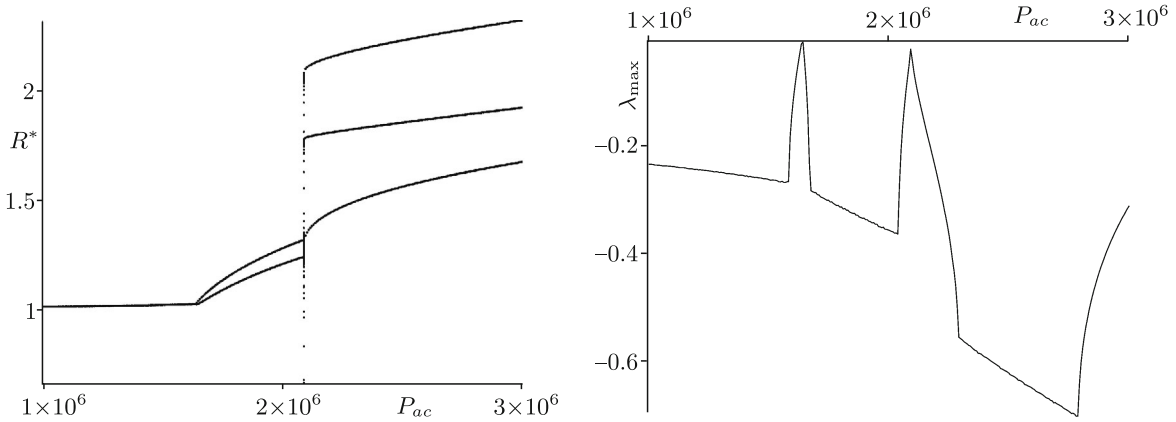

Fig. 19. Bifurcation diagram and $\lambda_{\max}$ for $\omega = 5.5 \cdot 10^7$, $P \in [1, 3]$ MPa.

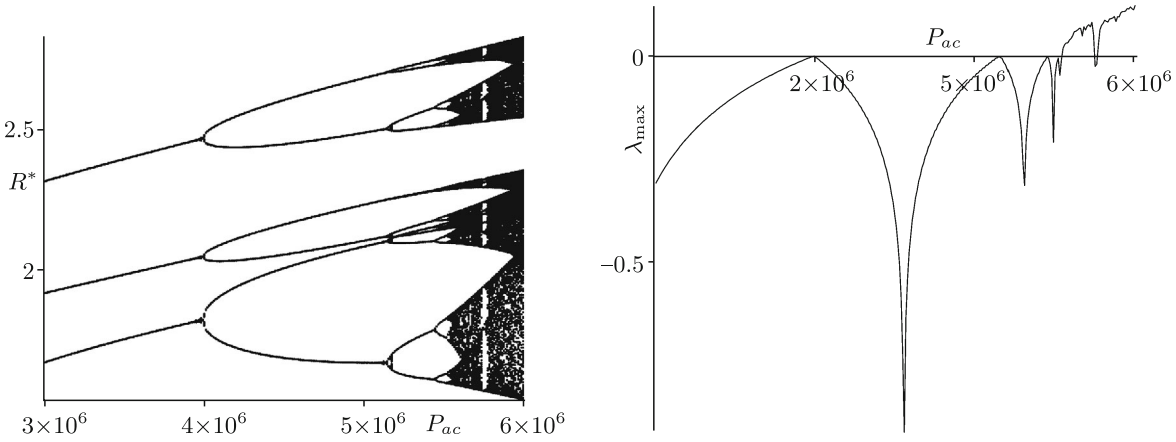

Fig. 20. Bifurcation diagram and $\lambda_{\max}$ for $\omega = 5.5 \cdot 10^7$, $P \in [3, 6]$ MPa.

the 3-periodic attractor emerges at $P_{ac} \approx 2.091$ MPa and the period-doubling bifurcation occurs at $P_{ac} \approx 2.101$ MPa (we performed calculations with much higher precision for the difference between these points to significantly exceed possible numerical errors). In our previous calculations the bifurcation points for different attractors did not coincide (see Figs. 11 and 12), even though they lay close to each other. Thus, we conclude that these two bifurcation points are likely different, but

located very close to each other. The emergence of the 3-periodic attractor looks quite similar to those in Fig. 14. With the increasing pressure, the 3-periodic attractor stays as it is for $P_{ac} \leqslant 3$ MPa, while the other one becomes chaotic after the period-doubling cascade. These attractors coexist until the chaotic one disappears in a crisis, and the 3-periodic attractor is the only remaining one. If we increase the P_{ac} still further (slightly higher than appears to be common in applications), we will observe the period-doubling cascade for this 3-periodic attractor (see Fig. 20). From all of the above, we can conclude that there is a lower boundary of frequencies under which the multistability is not possible for the range of pressures under investigation.

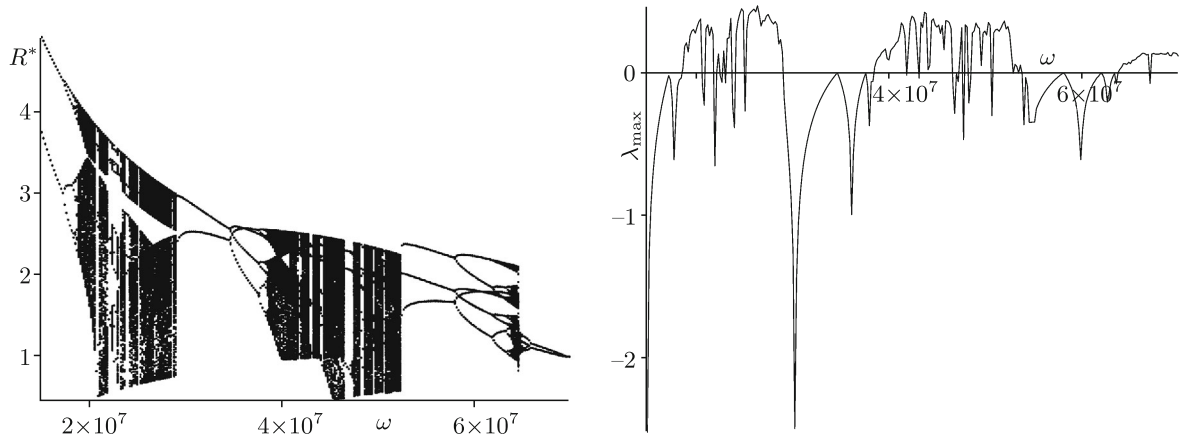

Fig. 21. Bifurcation diagram and $\lambda_{\max}$ for $P = 3$ MPa, $\omega \in [1.5, 7] \cdot 10^7$ s^{-1}, starting from the periodic attractor at the maximal frequency.

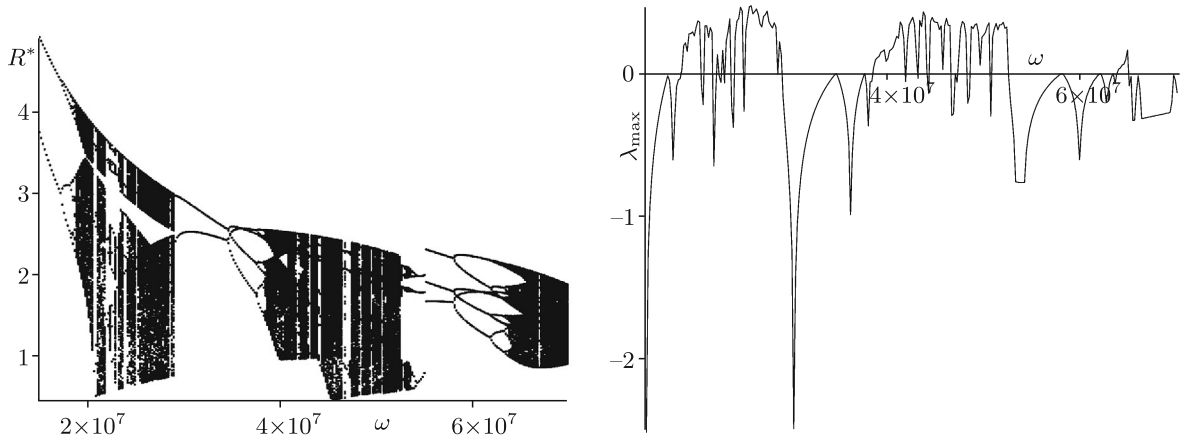

Fig. 22. Bifurcation diagram and $\lambda_{\max}$ for $P = 3$ MPa, $\omega \in [1.5, 7] \cdot 10^7$ s^{-1}, starting from the chaotic attractor at the maximal frequency.

For the next calculations we fix the pressure at $P_{ac} = 3$ MPa and vary ω in the same set as in Fig. 10. The bifuraction diagrams and the corresponding $\lambda_{\max}$ are shown in Figs. 21 and 22. The areas of chaos are largely expanded in comparison with Fig. 10. One could expect that to happen given the above-mentioned diagrams with varying pressures. The multistability phenomenon can be observed for the high frequencies in our range. We show two different diagrams to emphasize the fact of coexistence of a periodic and a chaotic attractor at the right end of the diagrams. To build the diagrams and the dependence of the $\lambda_{\max}$ on ω, we have used the continuation method with decreasing frequency sequences, starting from the different attractors at $\omega = 7 \cdot 10^7$ s^{-1}. These attractors were obtained from those we already had for $\omega = 6.9 \cdot 10^7$ s^{-1} and $P_{ac} = 3$ MPa (see Figs. 11, 13) by changing the control parameters with small steps.

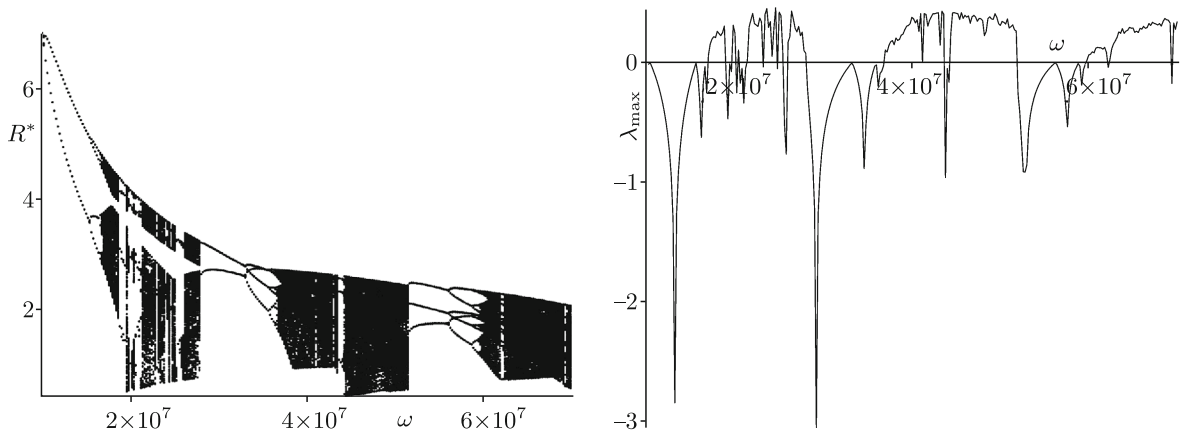

Fig. 23. Bifurcation diagram and $\lambda_{\max}$ $P = 3.5$ MPa, $\omega \in [1, 7] \cdot 10^7$ s^{-1}.

Finally, we consider the following parameters: $P = 3.5$ MPa, $\omega \in [1, 7] \cdot 10^7$ s^{-1}. The diagram and $\lambda_{\max}$ are provided in Fig. 23. We see that areas of chaos are prevailing over ranges of regular behavior. The multistability disappears for this pressure, and we observe a single attractor for all the frequencies in the range. Thus, there is a higher boundary of the pressures, after which the multistability does not exist in the system.

5. CONCLUSION

In this work we have studied three models describing the behavior of a bubble contrast agent: Eqs. (2.1), (2.3) and (2.4). The acoustic pressure and the driving frequency have been considered as the control parameters. In all of these models we have found complicated dynamics and the multistability phenomenon. We have demonstrated that the perpetual points method cannot always fully solve the initial values problem for these models. Another method we have used is based on the numerical continuation. By applying the last one, we could move from a region where the structure of coexisting attractors is simpler and easier to identify to other areas of the control parameters where it can be much more complicated. Also, it can help to understand how each of the attractors changes while passing through the bifurcations points.

We have demonstrated that, for the nonencapsulated bubble, complicated behavior like coexistence of a chaotic and a periodic attractor can be found for a relatively low acoustic pressure (see Fig. 1). If the pressure is increased, attractors with more complicated structure can develop in the areas where multistability takes place. On the contrary, for the encapsulated bubble, higher pressures are required for the system to exhibit such sort of complicated dynamics. In these models, the coexistence of periodic attractors becomes possible for lower pressures than the coexistence of a chaotic attractor with a periodic one. We have shown that in the set of the control parameters under investigation there exists a lower boundary of frequencies, under which the multistability is not possible. Also, we have demonstrated that there are both the lower and the higher boundaries of the acoustic pressure, in limits of which the multistability is possible. These boundaries depend on the frequency (see Figs. 11, 12, 18, 19, 23). Outside of these limits we have not found any coexisting attractors in the domain of parameters investigated in this paper. From the diagrams in Figs. 11, 12, 16–19, we can conclude that for lower frequencies chaotic behavior tends to emerge for lower pressures than it does for higher frequencies. On the other hand, for higher frequencies the system tends to exhibit the multistability phenomenon to a greater extent. We have provided regions of coexistence of different attractors for wide ranges of the control parameters along with areas where only one attractor exists (for example, only periodic or only chaotic motion is possible).

According to [3, 13], chaotic motion can be good for ultrasound diagnostics because the bubble response differs significantly from the echoes of surrounding tissues. We think that the coexistence of a periodic attractor with a chaotic one is not beneficial for applications. We make this conclusion, because this kind of multistability can lead to unpredictable behavior. We cannot control the initial conditions after the injection of contrast agents into the blood flow and can never know to which attractor the system will converge when we begin to apply the ultrasound field. Furthermore, there are a lot of sources of perturbations in the model, like finite measurement errors in the control

parameters, some sound waves propagating in the blood flow, etc. These disturbances can force the system to sharply shift from one attractor to another. Thus, the experimenter could observe a lot of sharp shifts between periodic and chaotic motion modes and vice versa. Therefore, we assume that the areas of the control parameters for which coexisting attractors are found should be avoided in applications.

ACKNOWLEDGMENTS

This work was supported by the Russian Science Foundation, grant number 17-71-10241.

REFERENCES

1. Szabo, Th. L., *Diagnostic Ultrasound Imaging: Inside Out,* 2nd ed., Cambridge: Academic Press, 2013.
2. Goldberg, B. B., Raichlen, J. S., and Forsberg, F., *Ultrasound Contrast Agents: Basic Principles and Clinical Applications,* London: Dunitz, 2001.
3. Hoff, L., *Acoustic Characterization of Contrast Agents for Medical Ultrasound Imaging,* Dordrecht: Springer, 2001.
4. Klibanov, A. L., Microbubble Contrast Agents: Targeted Ultrasound Imaging and Ultrasound-Assisted Drug-Delivery Applications, *Invest Radiol.,* 2006, vol. 41, no. 3, pp. 354–362.
5. Coussios, C. C. and Roy, R. A., Applications of Acoustics and Cavitation to Noninvasive Therapy and Drug Delivery, *Annu. Rev. Fluid Mech.,* 2008, vol. 40, pp. 395–420.
6. Strutt, J. W. (3rd Baron Rayleigh), On the Pressure Developed in a Liquid during the Collapse of a Spherical Cavity, *Philos. Mag. (6),* 1917, vol. 34, pp. 94–98.
7. Plesset, M. S., The Dynamics of Cavitation Bubbles, *J. Appl. Mech.,* 1949, vol. 16, pp. 277–282.
8. Faez, T., Emmer, M., Kooiman, K., Versluis, M., van der Steen, A., and de Jong, N., 20 Years of Ultrasound Contrast Agent Modeling, *IEEE Trans. Ultrason. Ferroelectr. Freq. Control.,* 2013, vol. 60, no. 1, pp. 7–20.
9. Doinikov, A. A. and Bouakaz, A., Review of Shell Models for Contrast Agent Microbubbles, *IEEE Trans. Ultrason. Ferroelectr. Freq. Control.,* 2011, vol. 58, no. 5, pp. 981–993.
10. Parlitz, U., Englisch, V., Scheffczyk, C., and Lauterborn, W., Bifurcation Structure of Bubble Oscillators, *J. Acoust. Soc. Amer.,* 1990, vol. 88, no. 2, pp. 1061–1077.
11. Behnia, S., Jafari, A., Soltanpoor, W., and Jahanbakhsh, O., Nonlinear Transitions of a Spherical Cavitation Bubble, *Chaos Solitons Fractals,* 2009, vol. 41, no. 2, pp. 818–828.
12. Macdonald, C. A. and Gomatam, J., Chaotic Dynamics of Microbubbles in Ultrasonic Fields, *Proc. Inst. Mech. Eng. C,* 2006, vol. 220, no. 3, pp. 333–343.
13. Carroll, J. M., Calvisi, M. L., and Lauderbaugh, L. K., Dynamical Analysis of the Nonlinear Response of Ultrasound Contrast Agent Microbubbles, *J. Acoust. Soc. Am.,* 2013, vol. 133, no. 5, pp. 2641–2649.
14. Doinikov, A. A., Aired, L., and Bouakaz, A., Acoustic Scattering from a Contrast Agent Microbubble near an Elastic Wall of Finite Thickness, *Phys. Med. Biol.,* 2011, vol. 56, no. 21, pp. 6951–6967.
15. Kudryashov, N. A. and Sinelshchikov, D. I., Analytical Solutions of the Rayleigh Equation for Empty and Gas-Filled Bubble, *J. Phys. A,* 2014, vol. 47, no. 40, 405202, 10 pp.
16. Kudryashov, N. A. and Sinelshchikov, D. I., Analytical Solutions for Problems of Bubble Dynamics, *Phys. Lett. A,* 2015, vol. 379, no. 8, pp. 798–802.
17. Kudryashov, N. A. and Sinelshchikov, D. I., On the Connection of the Quadratic Liénard Equation with an Equation for the Elliptic Functions, *Regul. Chaotic Dyn.,* 2015, vol. 20, no. 4, pp. 486–496.
18. de Jong, N., Hoff, L., Skotland, T., and Bom, N., Absorption and Scatter of Encapsulated Gas Filled Microspheres: Theoretical Considerations and Some Measurements, *Ultrasonics,* 1992, vol. 30, no. 2, pp. 95–103.
19. Marmottant, P., van der Meer, S., Emmer, M., Versluis, M., de Jong, N., and Hilgenfeldt, S., A Model for Large Amplitude Oscillations of Coated Bubbles Accounting for Buckling and Rupture, *J. Acoust. Soc. Am.,* 2005, vol. 18, no. 6, pp. 3499–3505.
20. Tu, J., Guan, J., Qiu, Y., and Matula, T. J., Estimating the Shell Parameters of SonoVue Microbubbles Using Light Scattering, *J. Acoust. Soc. Am.,* 2009, vol. 126, no. 6, pp. 2954–2962.
21. Keller, J. B. and Miksis, M., Bubble Oscillations of Large Amplitude, *J. Acoust. Soc. Am.,* 1980, vol. 68, no. 2, pp. 628–633.
22. Doinikov, A. A. and Bouakaz, A., Modeling of the Dynamics of Microbubble Contrast Agents in Ultrasonic Medicine: Survey, *J. Appl. Mech. Tech. Phys.,* 2013, vol. 54, no. 6, pp. 867–876; see also: *Prikl. Mekh. Tekhn. Fiz.,* 2013, vol. 54, no. 6, pp. 5–16.
23. Dudkowski, D., Jafari, S., Kapitaniak, T., Kuznetsov, N. V., Leonov, G. A., and Prasad, A., Hidden Attractors in Dynamical Systems, *Phys. Rep.,* 2016, vol. 637, pp. 1–50.
24. Dudkowski, D., Prasad, A., and Kapitaniak, T., Perpetual Points: New Tool for Localization of Coexisting Attractors in Dynamical Systems, *Internat. J. Bifur. Chaos Appl. Sci. Engrg.,* 2017, vol. 27, no. 4, 1750063, 11 pp.

25. Leonov, G. A., Kuznetsov, N. V., and Mokaev, T. N., Homoclinic Orbits, and Self-Excited and Hidden Attractors in a Lorenz-Like System Describing Convective Fluid Motion, *Eur. Phys. J. Special Topics,* 2015, vol. 224, no. 8, pp. 1421–1458.
26. Bizyaev, I. A., Borisov, A. V., and Mamaev, I. S., The Dynamics of Three Vortex Sources, *Regul. Chaotic Dyn.,* 2014, vol. 19, no. 6, pp. 694–701.
27. Borisov, A. V., Kazakov, A. O., and Pivovarova, E. N., Regular and Chaotic Dynamics in the Rubber Model of a Chaplygin Top, *Regul. Chaotic Dyn.,* 2016, vol. 21, nos. 7–8, pp. 885–901.
28. Borisov, A. V., Kazakov, A. O., and Sataev, I. R., Spiral Chaos in the Nonholonomic Model of a Chaplygin Top, *Regul. Chaotic Dyn.,* 2016, vol. 21, nos. 7–8, pp. 939–954.
29. Cash, J. R. and Karp, A. H., A Variable Order Runge – Kutta Method for Initial Value Problems with Rapidly Varying Right-Hand Sides, *ACM Trans. Math. Software,* 1990, vol. 16, no. 3, pp. 201–222.
30. Benettin, G., Galgani, L., Giorgilli, A., and Strelcyn, J.-M., Lyapunov Characteristic Exponents for Smooth Dynamical Systems and for Hamiltonian Systems: A Method for Computing All of Them: P. 1. Theory, *Meccanica,* 1980, vol. 15, pp. 9–20.
31. Ramasubramanian, K. and Sriram, M. S., A Comparative Study of Computation of Lyapunov Spectra with Different Algorithms, *Phys. D,* 2000, vol. 139, nos. 1–2, pp. 72–86.
32. Garashchuk, I. R., Kudryashov, N. A., and Sinelshchikov, D. I., Hidden Attractors in a Model of a Bubble Contrast Agent Oscillating near an Elastic Wall, *EPJ Web Conf.,* 2018, vol. 173, 06006, 4 pp.